Wavefront corrected light sheet microscopy in turbid media

H. I. C. Dalgarno, T. Čižmár, T. Vettenburg, J. Nylk, F. J. Gunn-Moore et al.

Additional information on Appl. Phys. Lett.
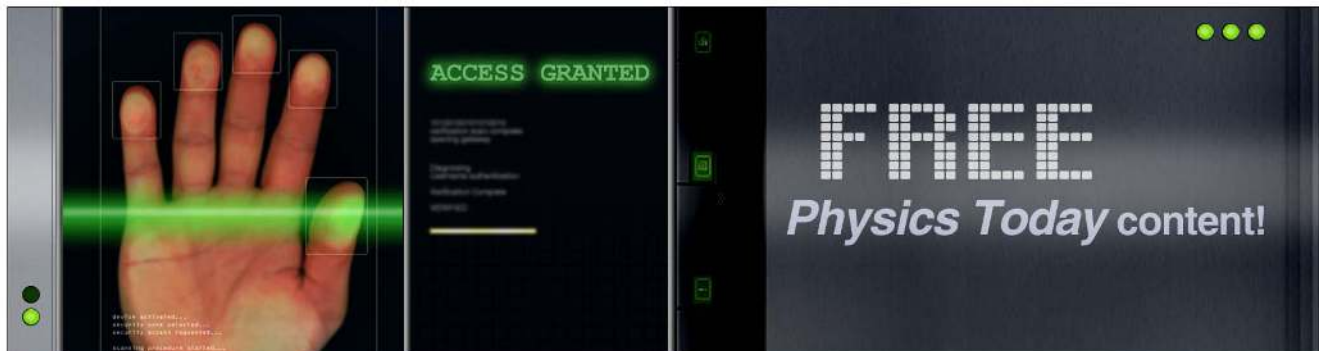
Wavefront corrected light sheet microscopy in turbid media

H. I. C. Dalgarno,[1,a)] T. Čižmár,[2,a)] T. Vettenburg,[1] J. Nylk,[1] F. J. Gunn-Moore,[3] and K. Dholakia[1]

[1]SUPA, School of Physics and Astronomy, University of St. Andrews, North Haugh, Fife KY16 9SS, Scotland, United Kingdom
[2]School of Medicine, Medical and Biological Sciences Building, University of St. Andrews, North Haugh, KY16 9TF, United Kingdom
[3]School of Biology, Medical and Biological Sciences Building, University of St. Andrews, North Haugh, KY16 9TF, United Kingdom

Light sheet microscopy is a powerful method for three-dimensional imaging of large biological specimens. However, its imaging ability is greatly diminished by sample scattering and aberrations. Optical clearing, Bessel light modes, and background rejection have been employed in attempts to circumvent these deleterious effects. We present an *in situ* wavefront correction that offers a major advance by creating an "optimal" light sheet within a turbid sample. Crucially, we show that no tissue clearing or specialized sample preparation is required, and clear improvements in image quality and depth resolution are demonstrated both in Gaussian and Bessel beam-based light sheet modalities. © *2012 American Institute of Physics.* [http://dx.doi.org/10.1063/1.4710527]

Light sheet microscopy (LSM) has emerged as a powerful wide-field fluorescence technique that has demonstrated exceptional high-resolution, high-speed, imaging in a wide variety of applications from developmental biology to colloidal studies.[1–4] In particular, it offers powerful capabilities for imaging larger biomedical specimens. Rapid single-axis scanning can create a "thin" two-dimensional light sheet that is then projected into the specimen at 90° to the detection objective axis. Both the Gaussian light sheet (GLS)[5] and Bessel Beam light sheet (BBLS)[6] imaging geometries have emerged as popular choices. Image quality and resolution in LSM are directly linked to the light sheet thickness and its uniformity across the imaged field of view (FOV). Both of these key properties are degraded in the presence of scattering and specimen-induced aberrations. Methods to circumvent these deleterious effects have included tissue clearing,[7] Bessel light modes,[8] and post-processing background suppression.[9] However, to truly extend LSM to a wider range of biomedical samples in their native state requires a significant improvement in overcoming aberrations as and where they arise within the sample. In this letter, we demonstrate how an *in situ* wavefront correction addresses this key point and allows the reconstruction of the beam profile exactly where one desires within the sample medium. It is important to stress that our method does not require any specialist sample preparation and crucially can be used to significantly improve any form of input light mode used in LSM, including both Gaussian and Bessel modes.

By decomposing an incident wavefront into an orthonormal basis, the scattering of the light can be understood and ultimately controllably shaped to produce both focusing and optical trapping deep within turbid media using an *in situ* probe.[10,11] This probe may be a fluorescent or scattering particle or, if the beam is imaged directly onto a CCD, a single pixel. For probes embedded within a turbid medium, such as fluorescent bio-markers in biological tissue, this technique provides full correction for both system and specimen-induced aberrations. Probe based wavefront measurement and correction has been demonstrated utilizing non-linear harmonic-generating particles,[12] direct imaging of the beam itself,[10] and on embedded fluorescent probes using interferometric[13] and Shack-Hartmann sensing.[14] An advantage of our method is its applicability to any type of probe; all that is required is that the probe produces an intensity signal.

In situ wavefront measurement and correction can be implemented using a spatial light modulator (SLM) to precompensate for unwanted aberrations and scattering effects. Analogously to phase conjugation, passage of the 'shaped' beam through the turbid medium thus forms an optimized focus at the position of the probe. To achieve this, a field decomposition into a series of orthogonal optical modes is defined in the plane of an SLM. The modes are then sequentially analyzed behind the randomizing medium by interference with a reference signal.[10,11] As the phase of a test mode is varied, the time-varying intensity of the probe is recorded and from this the optimal phase for that mode is deduced.[11] When the measured optimal phases of every mode are simultaneously applied, all modes will arrive at the specified point within the sample with the same phase, leading to optimal focusing of the whole light beam at that point. Optimized focusing of non-Gaussian beams is achieved by combining the optimized phases with the appropriate phase pattern or spatial filter—for example, a wavefront corrected Bessel beam is created by simply multiplying the pattern of optimized phases by a binary annular mask.[11]

In this letter, we apply *in situ* wavefront correction to the challenging case of LSM. We demonstrate resolution enhancement deep within turbid specimens using both GLS and BBLS imaging modalities.

Experimentally, a laser beam (Coherent Verdi V6, 6 W 532 nm) is expanded to fill the aperture of a single-axis acousto-optical deflector (AOD, Neos AOBD 45035-3) placed optically conjugate to the back aperture of the

---

a)Authors to whom correspondence should be addressed. Electronic mail: hicd2@st-andrews.ac.uk and tc51@st-andrews.ac.uk.
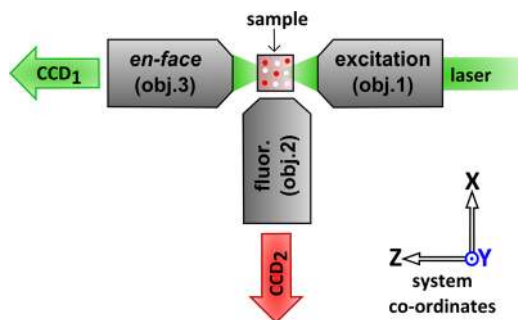
FIG. 1. Experimental configuration of the excitation and detection objectives (top-view).

excitation objective (Mitutoyo $20\times /0.42$, Fig. 1 (obj. 1)). The AOD rapidly scans the first diffraction order beam to form a light sheet within the sample volume, parallel to the image plane (y,z) of the fluorescence detection objective (Newport $20\times /0.4$, Fig. 1(obj. 2)). Phase modulation of the beam is achieved by placing an SLM (Hamamatsu LCOS X10468-04) in a plane conjugated to both the AOD and the excitation objective. Appropriate optics ensure overfilling of the active area of the SLM and the back aperture of the objective respectively. A major advantage of our system is the flexibility afforded by employing an SLM to produce and correct both Gaussian and Bessel modes; this allows dynamic switching of the light sheet mode for convenient selection of the optimal beam type for a given application or sample. A third objective (Mitutoyo $50\times /0.55$, Fig. 1 (obj. 3)) permits visualization of the beam's *en face* profile. The data are recorded with two CCD cameras (Basler piA640-210 gm). The sample is mounted on a three-axis motorized translation stage (Mad City Labs, Nano-LP200) to permit accurate positioning of the sample with respect to the light sheet and the focal plane of objective 2 (Fig. 1).

Wavefront measurement and subsequent correction for the optical system aberrations were achieved using the image of the focused beam from objective 1 (Fig. 1) as the correction probe. A stack of *en face* images, collected along the propagation axis (z), provided profiles of the scanning GLS and BBLS (Fig. 2). *En face* images of both beams at the

Gaussian beam waist (Figs. 2(a) and 2(d)) show that, with *in situ* correction, a diffraction-limited light sheet thickness of 0.8 μm was achieved. Profiles in the (x,z) and (y,z) planes (Figs. 2(b), 2(e) and 2(c), 2(f), respectively) were reconstructed from the image stack. As expected, the BBLS has a significantly longer axial (z-axis) extent where the core size is constant compared to the GLS. As Fig. 2(f) shows, this results in a more uniform excitation illumination across the FOV of the fluorescence detection objective (Fig. 1 (obj. 2)). However, in addition to the main light sheet created by the BB core, the side-lobes produce additional sheets which reduce image contrast due to the increased background.[8] Multi-photon excitation offers a solution, as the influence of these side-lobes is suppressed.[6]

To evaluate the correction ability of our system in turbid media, tissue phantoms of varied scattering and abberative properties were used. These comprised of a suspension of dried polystyrene and/or silica micro-particles in polydimethylsiloxane (PDMS) injected into square-profile borosilicate glass capillaries (Vitrocell 8250-100, inner/outer width 500/700 μm). Mixtures of red fluorescent polystyrene beads (Duke R100 or Duke R900, $\varnothing = 1\,\mu m$ or $\varnothing = 0.93\,\mu m$, respectively) and non-fluorescent polystyrene or silica beads ($\varnothing = 2\,\mu m$–$11\,\mu m$) were used. The refractive index ratio (m) of silica micro-particles to PDMS is 1.04, which is a reasonable approximation for scatterers in cells and tissues.[16] Polystyrene beads, which give $m = 1.13$, are consequently expected to be more scattering than typical tissues.[17] The scattering coefficient (μ_s) of each sample was determined by measuring the total transmitted ballistic intensity ($\sum I_{test}$) relative to the transmission of a reference sample (empty capillary, total transmission $\sum I_{ref}$). This was repeated for six random positions along the capillary to obtain an average μ_s. Experimentally, the collimated laser beam ($\varnothing = 532\,nm, \varnothing = 2.25\,\mu m$) passed through a 200 μm aperture and subsequently through the capillary under test. At a distance of 425 mm from the capillary, a 1 mm iris and CCD selected and captured a small central portion of the transmitted light. The scattering coefficient is given by $\mu_s = \ln(\sum I_{test}/\sum I_{ref})/d$, where d is the depth of the scattering material (500 μm). The corresponding reduced
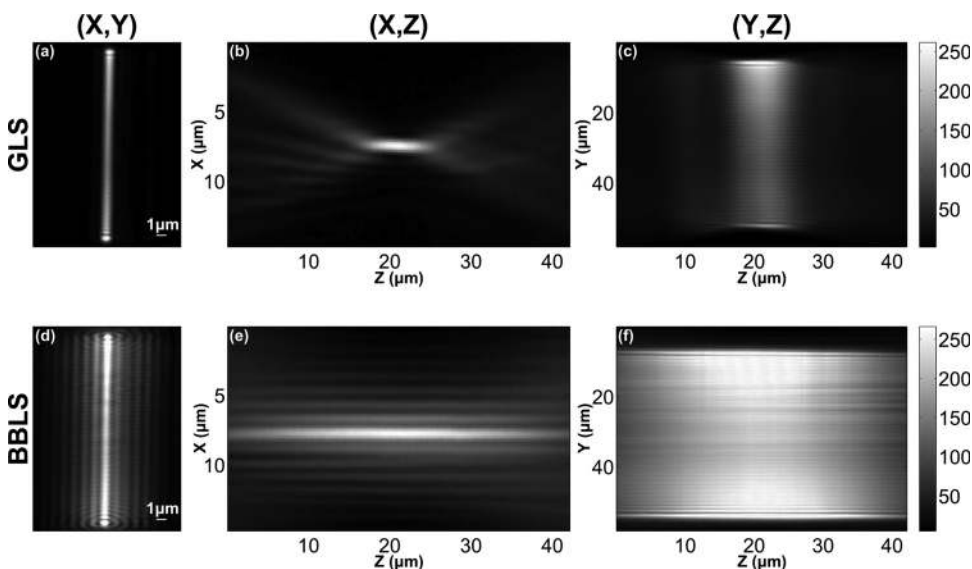

FIG. 2. *En face* images of the GLS (a) and BBLS (d) taken at the Gaussian beam waist, with wavefront correction. The light sheet thickness [width in x-axis: (b) and (e)] and intensity profile in the LSM detection axis [(y,z) plane: (c) and (f)] for GLS and BBLS are reconstructed from a sequence of *en face* images captured along the propagation axis (z). Intensity scale-bars shown apply to all plots (a)-(f)

scattering coefficients (μ'_s) were calculated from Mie theory.[18,19] Samples used in this study had measured scattering coefficients of $\mu_s = 22$–$138 \, cm^{-1}$ ($\mu'_s = 0.25$–$17.6 \, cm^{-1}$). The corresponding mean free paths (MFPs = $1/\mu_s$), covered a range of $73 - 222 \, \mu m$. These tissue phantoms provide reasonable approximations to biological tissues, where expected MFPs are of the order of $100 \, \mu m$,[20] and the expected range for soft-tissue scattering of $\mu_s = 100$ to $1000 \, cm^{-1}$.[21]

A capillary filled only with clear PDMS was used to determine the "system correction" for the complete optical pathway.[11] The laser was focused at the rear wall of the capillary (closest to obj. 3, Fig. 1), and its image (CCD$_1$) used as the correction probe (probe depth = $500 \, \mu m$). The system correction sample was then replaced by a tissue phantom. In the selected example shown (Fig. 3), this contained a mixture of $\varnothing = 1 \, \mu m$ fluorescent polystyrene and $\varnothing = 6.8 \, \mu m$ silica beads in PDMS ($\mu_s = 53 \, cm^{-1}$, $\mu'_s = 0.36 \, cm^{-1}$, probe depth equivalent to 2.6 MFP). The intensity profiles of the system corrected GLS and BBLS beams were measured, and their respective average intensities (I$_0$) calculated. A second wavefront correction measurement determined the total correction required for both system and sample-induced aberrations ("full correction"). In Figures 3(a) and 3(b), cross-sections along the beam scanning direction (y-axis) of the in-focus *en face* image, normalized by I$_0$, compare the performance of the system and fully corrected GLS and BBLS in the tissue phantom sample. Normalization by I$_0$ shows the intensity enhancement produced when full correction is applied. In this case, the transmitted intensity for the GLS beam with full correction is approximately a factor of

four greater at the correction probe position (y = 0, Figs. 3(a) and 3(b)), compared to the BBLS which is enhanced by a factor of approximately two. Although the BB peak intensity on axis is lower, the benefit of the enhancement is of course distributed over a larger area due to its extended FOV. Both beams produce a peaked intensity profile centered at the correction probe. The peak width indicates the range over which an individual correction is valid and depends on the properties of the individual sample. This was previously described as the "optical memory" effect[22] and is analogous to the isoplanatic patch found in atmospheric adaptive optics.[15] This experiment was repeated on a range of samples, and confirmed that samples with higher scattering and increased aberrative properties correspondingly have a smaller "optical memory" range. The samples tested spanned a range of $\mu_s = 37$–$132 \, cm^{-1}$ ($\mu'_s = 0.25$–$17.6 \, cm^{-1}$), the FWHMs of the corrected peaks were found to be between 2 and 5 μm, and in each case, the FWHM of the GLS and BBLS beams matched to within 10%.

Figures 3(c) and 3(d) show the evolution of the light sheet as it was scanned through the sample along the x-axis. GLS cross-sections recorded at CCD$_1$ were observed to have a double-Gaussian profile; a sharply peaked Gaussian in the center overlapped by a broader, lower intensity, Gaussian created by scattering and residual aberrations. The signal-to-noise ratio (SNR) is defined as the intensity ratio of these Gaussian peaks and shown in Figure 3(c). Figure 3(d) plots the width of the central GLS Gaussian peak showing that without full correction the light sheet waist is broad and varies randomly across the lateral scan range. In contrast,
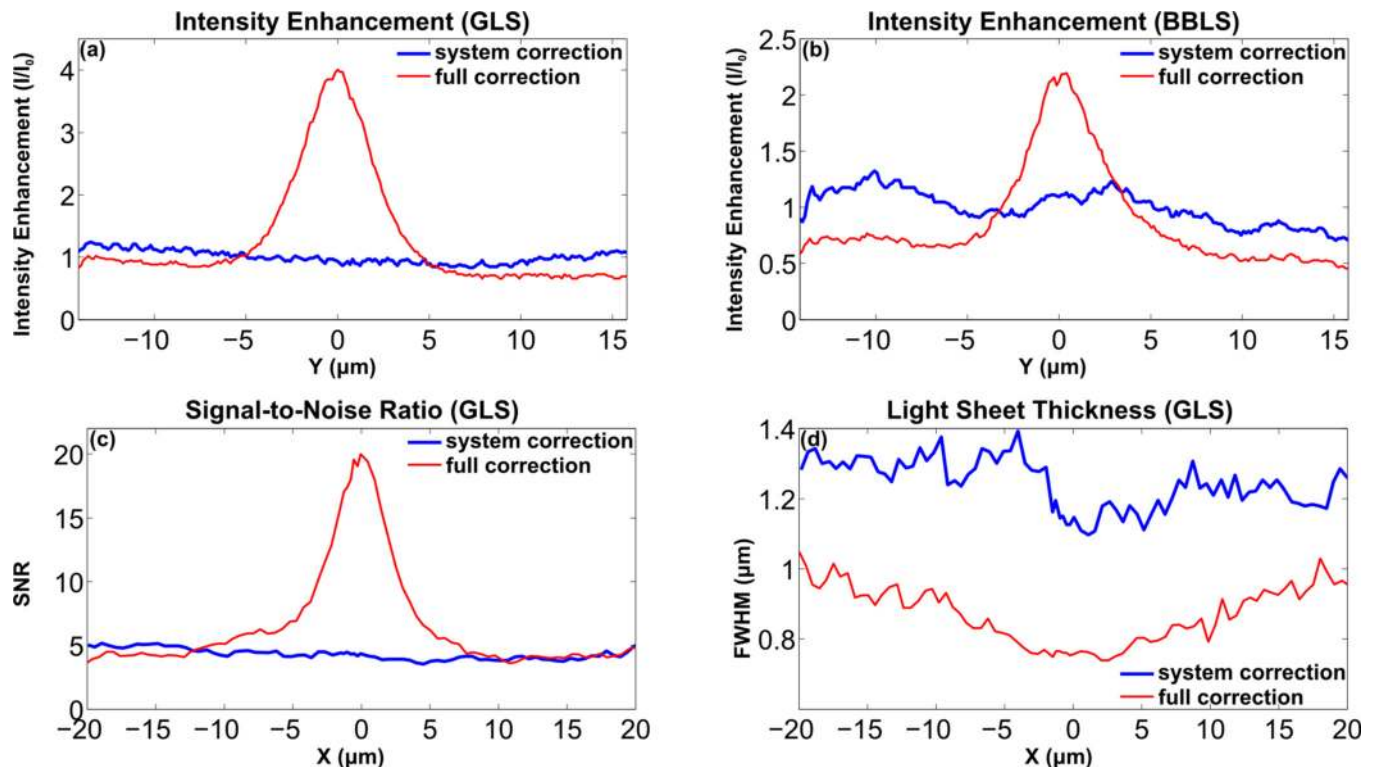

FIG. 3. Cross-sections (y-axis) of the *en face* image at focus, normalized by the average intensity of the system corrected beam in the phantom sample ($\mu_s = 53 \, cm^{-1}$, $\mu'_s = 0.36 \, cm^{-1}$, probe depth equivalent to 2.6 MFP). These show the intensity enhancement afforded by full correction and the vertical scan region over which this correction remains valid (central peak, full corrected profiles) for the GLS (a) and BBLS (b). The ratio of light sheet intensity to the scattered background (SNR) as a function of lateral-scan position is shown (c). Light sheet thickness (FWHM) is plotted as a function of lateral-scan position (x-axis) relative to the correction probe position (d).

with full correction, the waist is minimized and diffraction-limited at the probe position ($x = 0$). It remains narrow across the region where the correction is valid ($\approx 10\,\mu m$). This result is consistent with the findings of Figs. 3(a)–3(c) and thus demonstrates the isotropic characteristics of this sample. In every sample, both intensity enhancement and diffraction-limited light sheet width were achieved. This was so even in the extreme case where the probe depth was equivalent to 6.6 MFP, where intensity enhancement by a factor of three was observed for the GLS. This represents a dramatic improvement in maximum penetration depth over the expected limit for LSM, which is approximately 1 MFP for biological tissues.[20]

In situ wavefront measurement and correction were implemented in the LSM detection path using a fluorescent probe particle ($\emptyset = 0.93\,\mu m$) positioned in the center of the focused light sheet. The correction method is as previously described, except that here the variation of the bead fluorescence as the test mode phase varies provides the measurement. The bead size is chosen to be close to the resolution of the excitation objective ($0.8\,\mu m$, diffraction-limited light sheet thickness). Critically, since the wavefront measurement is made by integrating the intensity over the probe, it must also be smaller than the minimum fringe period of the interference pattern ($2.75\,\mu m$ in our system), which is produced by modes at the outermost edges of the pupil. System-only correction was obtained for a sample capillary containing a low concentration of $0.93\,\mu m$ diameter fluorescent beads in PDMS. To ensure fair comparison, this system correction was adjusted as required to add tilt and defocus to ensure the system and fully corrected beams both focused exactly on the correction probe during imaging. To compare the GLS and BBLS imaging with depth, image stacks were collected over a $50\,\mu m$ depth (x) range, in 100 nm steps, for a range of samples to test performance with varying levels of scattering and aberration.

Figure 4 shows results from a tissue phantom comprising $0.93\,\mu m$ diameter fluorescent polystyrene beads and $5\,\mu m$ diameter silica beads in PDMS ($\mu_s = 46\,cm^{-1}$, $\mu'_s = 0.28\,cm^{-1}$, propagation depth to probe equivalent to 1.2 MFP). Figures 4(a) and 4(b) are maximum-intensity projections obtained for

a GLS depth-stack in the region of the fluorescent correction probe (circled particle, Figs. 4(a) and 4(b)). A significant enhancement of intensity and resolution is noted when full *in situ* wavefront correction is applied (Fig. 4(b)); intensity enhancement by factors of 2.8 and 1.7, and reductions of the FWHM by factors of 3.7 and 1.4 are seen for the GLS and BBLS, respectively. To test the robustness of the technique, this experiment was repeated with a range of samples for probe depths of up to 3.4 MFP. It was found that this method works in every case. However, the level of improvement varies due to the random nature of the particle distribution within the sample; the worse the local aberrations, the greater the benefits gained by performing a full correction. Figures 4(c) and 4(d) show depth cross-section profiles of the correction probe bead. It can be seen that the full corrected GLS provides the highest resolution, clearly outperforming the corrected BBLS. The superior resolution of the GLS does, however, come at a cost; in our system, the GLS provides approximately $10\,\mu m$ wide fluorescence image FOV, compared to $50\,\mu m$ for the BBLS. This highlights that, for a given sample and excitation depth, there exists an important trade-off between resolution and FOV.

A very detailed comparison of GLS and BBLS imaging modalities is outside the scope of this letter; however, we offer the following remarks in this regard. A disadvantage of BBLS compared to GLS is that a significant proportion of the power is diverted into the outer rings of the BB, reducing photometric efficiency whilst increasing out-of-focus background and sample exposure to radiation that does not contribute to imaging. Multi-photon excitation mitigates the latter, at the added cost and complexity of a suitable multi-photon source.[6] The advantages of using a BBLS over a GLS are its remarkable self-healing ability and extended FOV, which is further improved by wavefront correction. In the single photon regime, wavefront corrected GLS delivers higher resolution and focal intensity for a smaller FOV. These factors should be taken into consideration when choosing the most appropriate beam to achieve optimum performance for a given LSM application.

We have demonstrated the implementation of wavefront correction in GLS and BBLS imaging and have shown
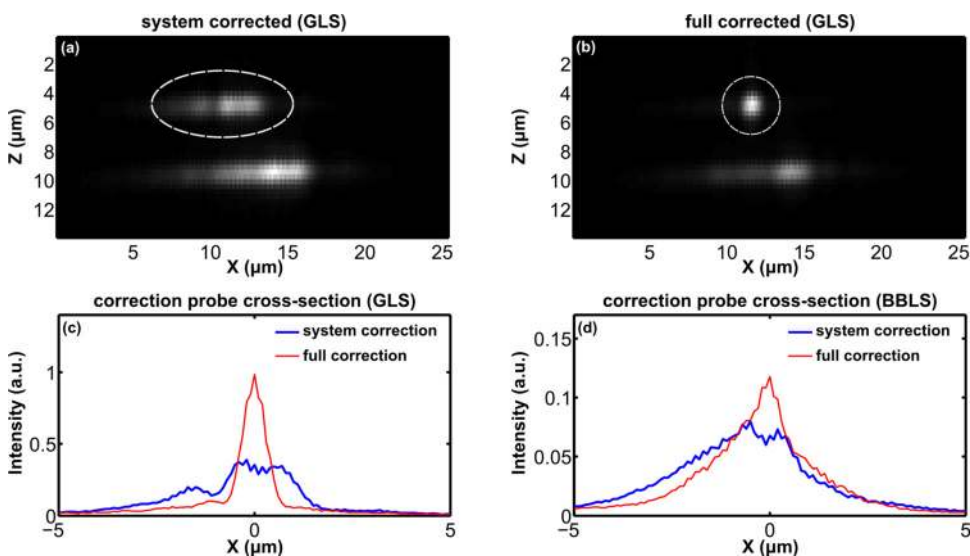

FIG. 4. Fluorescence image wavefront correction in LSM. Maximum-intensity projections [(a) and (b)] of an image depth stack for the GLS with both system-only and full *in situ* wavefront correction (correction probe circled) in a turbid sample ($\mu_s = 46\,cm^{-1}$, $\mu'_s = 0.28\,cm^{-1}$, propagation depth to probe equivalent to 1.2 MFP). Intensity and depth resolution enhancement is compared for system-only and full correction in the GLS and BBLS modes [(c) and (d)].

diffraction-limited performance deep within turbid tissue phantom samples at depths of up to six times the MFP. Optical memory effects, resulting from the individual sample properties, were shown to allow isotropic enhancement covering a range of up to 10 μm for a single correction measurement. This study clearly shows that by correcting the entire optical pathway and regardless of incident beam choice, LSM image quality and resolution are dramatically improved. Further optimization by enhancement of the lateral resolution could be achieved by including adaptive optics correction within the fluorescence imaging pathway.[23] *In vivo* applications will require high speed wavefront measurement and correction; the method presented here is limited by the refresh rate of the SLM and may be extended to real-time correction by using scanning mirrors or an AOD to scan the modes instead.[24] By correcting for the entire optical pathway, 4D LSM imaging will extend deeper, more efficiently, and with greater resolution into *in vivo* biological specimens and tissues.

[1] J. Huisken, J. Swoger, F. D. Bene, J. Wittbrodt, and E. H. K. Stelzer, Science **305**, 1007 (2004).
[2] J. Huisken and D. Y. R. Stainier, Development **136**, 1963 (2009).
[3] T. F. Holekamp, D. Turaga, and T. E. Holy, Neuron **57**, 661 (2008).
[4] J. G. Ritter, R. Veith, J. P. Siebrasse, and U. Kubitscheck, Opt. Express **16**, 7142 (2008).
[5] P. J. Keller, A. D. Schmidt, J. Wittbrodt, and E. H. K. Stelzer, Science **322**, 1065 (2009).
[6] T. A. Planchon, L. Gao, D. E. Milkie, M. W. Davidson, J. A. Galbraith, C. G. Galbraith, and E. Betzig, Nat. Methods **8**, 417 (2011).
[7] H. U. Dodt, U. Leischner, A. Schierloh, N. Jährling, C. P. Mauch, K. Deininger, J. M. Deussing, M. Eder, W. Zieglgänsberger, and K. Becker, Nat. Methods **4**, 331 (2007).
[8] F. O. Fahrbach, P. Simon, and A. Rohrbach, Nature Photon. **4**, 780 (2010).
[9] J. Mertz and J. Kim, J. Biomed. Opt. **15**, 016027 (2010).
[10] I. M. Vellekoop, A. Lagendijk, and A. P. Mosk, Nature Photon. **4**, 320 (2010).
[11] T. Čižmár, M. Mazilu, and K. Dholakia, Nature Photon. **4**, 388 (2010).
[12] C.-L. Hsieh, Y. Pu, R. Grange, G. Laporte, and D. Psaltis, Opt. Express **18**, 20723 (2010).
[13] I. M. Vellekoop, E. G. van Putten, A. Lagendijk, and A. P. Mosk, Opt. Express **16**, 67 (2008).
[14] O. Azucena, J. Crest, J. Cao, W. Sullivan, P. Kner, D. Gavel, D. Dillon, S. Olivier, and J. Kubby, Opt. Express **18**, 17521 (2010).
[15] R. K. Tyson, *Principles of Adaptive Optics* (Academic, San Diego, USA, 1991).
[16] J. R. Mourant, J. P. Freyer, A. H. Hielscher, A. A. Eick, D. Shen, and T. M. Johnson, Appl. Opt. **37**, 3586 (1998).
[17] J. M. Schmitt and A. Knüttel, J. Opt. Soc. Am. A **14**, 1231 (1997).
[18] R. Graaff, J. G. Aarnoudse, J. R. Zijp, P. M. A. Sloot, F. F. M. de Mul, J. Greve, and M. H. Koelink, Appl. Opt. **31**, 1370 (1992).
[19] B. Beauvoit, T. Kitai, and B. Chance, Biophys. J. **67**, 2501 (1994).
[20] V. Ntziachristos, Nat. Methods **7**, 603 (2010).
[21] A. P. Castano, T. N. Demidova, and M. R. Hamblin, Photodiagn. Photodyn. Ther. **1**, 279 (2004).
[22] I. Freund, M. Rosenbluh, and S. Feng, Phys. Rev. Lett. **61**, 2328 (1988).
[23] D. Turaga and T. E. Holy, Appl. Opt. **49**, 2030 (2010).
[24] M. Cui, Opt. Express **19**, 2989 (2011).